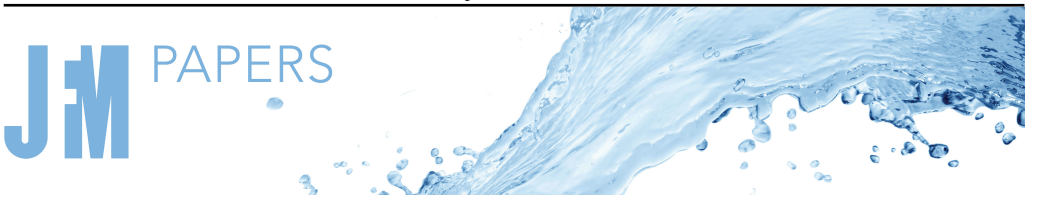
J. Fluid Mech. (2025), *vol.* 1024, A37, doi:10.1017/jfm.2025.10895



A diffuse-interface Marangoni instability

Xiangwei Li[1], **Dongdong Wan**[2], **Haohao Hao**[1], **Christian Diddens**[3], **Mengqi Zhang**[2] **and Huanshu Tan**[1]

[1]Multicomponent Fluids Group, Center for Complex Flows and Soft Matter Research, Department of Mechanics and Aerospace Engineering, Southern University of Science and Technology, Shenzhen, 518055 Guangdong, PR China

[2]Department of Mechanical Engineering, National University of Singapore, 9 Engineering Drive 1, 117575 Singapore, Republic of Singapore

[3]Physics of Fluids Department, Max-Planck Center Twente for Complex Fluid Dynamics and J. M. Burgers Centre for Fluid Dynamics, University of Twente, P. O. Box 217, 7500AE Enschede, The Netherlands

Corresponding author: Huanshu Tan, tanhs@sustech.edu.cn

(Received 11 June 2025; revised 31 August 2025; accepted 13 October 2025)

We investigate a novel Marangoni-induced instability that arises exclusively in diffuse fluid interfaces, that is absent in classical sharp-interface models. Using a validated phase-field Navier–Stokes–Allen–Cahn framework, we linearise the governing equations to analyse the onset and development of interfacial instability driven by solute-induced surface tension gradients. A critical interfacial thickness scaling inversely with the Marangoni number, $\delta_{cr} \sim Ma^{-1}$, emerges from the balance between advective and diffusive transport. Unlike sharp-interface scenarios where matched viscosity and diffusivity stabilise the interface, finite thickness induces asymmetric solute distributions and tangential velocity shifts that destabilise the system. We identify universal power-law scalings of velocity and concentration offsets with a modified Marangoni number Ma_δ, independent of capillary number and interfacial mobility. A critical crossover at $Ma_\delta \approx 590$ distinguishes diffusion-dominated stabilisation from advection-driven destabilisation. These findings highlight the importance of diffuse-interface effects in multiphase flows, with implications for miscible fluids, soft matter, and microfluidics where interfacial thickness and coupled transport phenomena are non-negligible.

Key words: Marangoni convection, interfacial flows (free surface), instability

1. Introduction

Marangoni instability, arising from the transverse mass transfer of surface-active species across a fluid interface (Sternling & Scriven 1959; Kovalchuk & Vollhardt 2006; Schwarzenberger *et al.* 2014), plays a fundamental role in multicomponent flow

© The Author(s), 2025. Published by Cambridge University Press.

https://doi.org/10.1017/jfm.2025.10895 Published online by Cambridge University Press

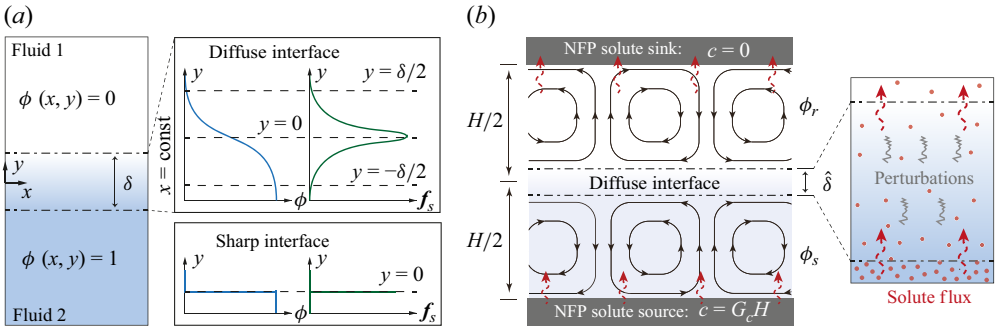


Figure 1. (*a*) Two-liquid-layer system with a constant solute gradient ∇c in the y-direction, modelled with either a diffuse interface or a sharp interface. (*b*) Marangoni instability induced by transverse solute mass transfer in a diffuse-interface two-layer system.

systems, such as evaporating droplets (Tan *et al.* 2016; Lohse & Zhang 2020; Diddens, Dekker & Lohse 2024), self-motived droplets (Levich & Krylov 1969; Michelin 2023), microextraction solutions (Eckert *et al.* 2012; Mitra *et al.* 2020) and liquid films (Darhuber & Troian 2003; Sultan, Boudaoud & Amar 2005). Its onset and evolution are governed by fluid property contrasts, particularly viscosity and mass diffusivity ratios between the interacting layers. Traditional linear stability analysis, based on an idealised sharp and non-deformable interface, establishes critical instability criteria (Sternling & Scriven 1959; Reichenbach & Linde 1981). However, direct numerical simulations (DNS) with a finite thickness, deformable interface validate these criteria while also revealing that excessive interface thickness can itself induce Marangoni instability (Verschueren, Van De Vosse & Meijer 2001; Li *et al.* 2025). This study seeks to further clarify the role of interface thickness in Marangoni instability and the underlying mechanisms.

A perfectly sharp fluid interface – one with zero thickness – does not exist. Even in immiscible liquids, the phase transition region spans nanometre scales (Mitrinović *et al.* 2000; Senapati & Berkowitz 2001). Jump conditions approximate the interface by neglecting continuous variation of properties across it (Scardovelli & Zaleski 1999; Reder *et al.* 2024) if the system size is much larger than the interfacial thickness $\hat{\delta}$. However, this assumption breaks down when $\hat{\delta}$ becomes comparable to the length scale of interest – such as in near-critical, partial miscible or submicron systems (Cahn & Hilliard 1958; Stanley 1971; Joseph *et al.* 1993; Anderson, McFadden & Wheeler 1998). In such cases, the transition occurs over a finite region still large compared with the molecular scale, motivating the diffuse-interface concept originally introduced by Rayleigh (1892) and van der Waals (1893) (figure 1*a*). This thickness can become relevant in small-scale complex fluids, such as polymer solutions and colloidal suspension (Truzzolillo & Cipelletti 2017; Bergfreund *et al.* 2021; Liu *et al.* 2021), where interfacial transport strongly affects the dynamics. Here, property variation within the interface can no longer be ignored (Cahn & Hilliard 1958).

Interfacial surface tension arises from tangential forces across the finite-thickness transition layer between two fluids, where anisotropic intermolecular forces act parallel to the interface (Berry 1971; Marchand *et al.* 2011). Surface-active solutes locally reduce tension according to a first-order approximation, $\gamma = \gamma_0 - \beta c$, where γ denotes the local interfacial tension with γ_0 as its reference value when the solute concentration c is zero, and β is a proportionality constant. While classical theories assume a sharp interface, the concept of solute-dependent interfacial tension extends to finite-thickness interfaces, where surface force $\boldsymbol{f}_s$ may develop heterogeneously across sublayers (figure 1*a*

https://doi.org/10.1017/jfm.2025.10895 Published online by Cambridge University Press

inset), driving localised solutal Marangoni flows (Anderson *et al.* 1998; Hao *et al.* 2025). These flows typically form symmetric convection rolls centred at stagnation points (figure 1*b*), and their multiscale interactions lead to interfacial turbulence (Ruckenstein & Berbente 1964). The linear theory by Sternling & Scriven (1959), based on the sharp-interface model, highlights the roles of viscosity and diffusivity ratios between source (ϕ_s) and receiver (ϕ_r) fluids, but is intrinsically incapable of capturing the coupled process (Manikantan & Squires 2020) within diffuse interfaces (figure 1*b* inset). Multicomponent multiphase flows – including surfactant-laden interfaces and multicomponent drops (Lohse & Zhang 2020; Michelin 2023; Hao *et al.* 2026) – have recently attracted renewed interest, and their relevance underscores the importance of examining how interfacial thickness influences the onset and development of Marangoni instabilities.

Phase-field methods, derived from free-energy formulations (Cahn & Hilliard 1958; Anderson *et al.* 1998; Jacqmin 1999), provide a continuous framework well suited to capture such finite-thickness effects. Interface distortion is regulated by mobility M_ϕ, balancing anti-diffusion and convection of the phase field ϕ (Demont, Stoter & Van Brummelen 2023); as $\hat{\delta}$ decreases, solutions converge to the sharp-interface limit (Magaletti *et al.* 2013). The physics-based formulation and asymptotic consistency not only make the phase-field approach ideal for uncovering interfacial-thickness-induced Marangoni instabilities, but also provide a means to assess whether the observed instability reflects genuine physical behaviour or arises as an artefact of the diffuse-interface formulation.

The paper is organised as follows. Section 2 introduces the phase-field formulation and its linearisation. Section 3 identifies the diffuse-interface-specific instability, establishes a scaling law for critical thickness, and elucidates underlying mechanisms via interface-offset analysis. Section 4 concludes with key findings and physical implications.

2. Problem formulation and linearisation

We use a validated phase-field Navier–Stokes–Allen–Cahn (NSAC) model to study solute-driven interfacial instability (Li *et al.* 2025). A brief description follows.

As depicted in figure 1(*b*), the system is characterised by a solute concentration gradient G_c oriented normal to a diffuse interface separating two fluid phases. These fluids are denoted by ϕ_s and ϕ_r, corresponding to the solute-supplying and solute-receiving phases, respectively. Both phases are confined between two flat, no-flow-penetration (NFP) boundaries, while periodic boundary conditions apply laterally. The characteristic length is defined as one quarter of the spacing distance, i.e. $L = H/4$. The interface is captured using the conservative Allen–Cahn equation in dimensionless form, which accounts for advective transport by the flow field $\boldsymbol{u} = (u(\boldsymbol{x}, t), v(\boldsymbol{x}, t))$,

$$\frac{\partial \phi_j}{\partial t} + \nabla \cdot \left(\phi_j \boldsymbol{u}\right) = \frac{1}{Pe_\phi}\left\{\nabla \cdot \left[\nabla \phi_j - B\phi_j\left(1-\phi_j\right)\frac{\nabla \phi_j}{\left|\nabla \phi_j\right|}\right] + \alpha_j\right\}, \tag{2.1}$$

where $j = s, r$ (no j summation), and $B = [4\,\mathrm{artanh}(1-2\delta_n)]/\delta$ controls the dimensionless interfacial thickness $\delta = \hat{\delta}/L$, and δ_n defines the numerically resolvable transition width. The equilibrium phase-field profile takes the form $\phi_{eq} = \{1 - \tanh[(y - 2L)B/2]\}/2$ (figure 1*a* inset). The Lagrange multipliers α_j enforce the constraint of $\phi_s + \phi_r = 1$.

The governing equations for fluid momentum and solute transport in dimensionless form are given by

https://doi.org/10.1017/jfm.2025.10895 Published online by Cambridge University Press

$$\frac{\partial \boldsymbol{u}}{\partial t} + \boldsymbol{u}\cdot\nabla\boldsymbol{u} = \frac{Sc}{Ma}\left\{-\nabla p + \nabla\cdot\left[\eta\left(\nabla\boldsymbol{u} + (\nabla\boldsymbol{u})^{\mathrm{T}}\right)\right] + \frac{\boldsymbol{f}_s}{Ca}\right\}, \quad 0 = \nabla\cdot\boldsymbol{u}, \tag{2.2a}$$

$$\frac{\partial c}{\partial t} = \frac{1}{Ma}\nabla\cdot[D(\nabla c)] - \nabla\cdot(c\boldsymbol{u}), \tag{2.2b}$$

where p denotes the pressure, the surface force effect is represented via a body force term $\boldsymbol{f}_s(x, y) = (1/2)[\gamma(\kappa_s\boldsymbol{n}_s + \kappa_r\boldsymbol{n}_r) + (\boldsymbol{I}_s - \boldsymbol{n}_s\boldsymbol{n}_s + \boldsymbol{I}_r - \boldsymbol{n}_r\boldsymbol{n}_r)\nabla\gamma]W$, with $\boldsymbol{n}_j = \nabla\phi_j/|\nabla\phi_j|$, $\kappa_j = -\nabla\cdot\boldsymbol{n}_j$ and $(\boldsymbol{I}_j - \boldsymbol{n}_j\boldsymbol{n}_j)\cdot\nabla$ representing the surface gradient operator in terms of phase field ϕ_j. This expression is parallel to the classical Boussinesq–Scriven surface traction model (Scriven 1960). The surface force term is only active within the diffuse interface, as the localisation function $W(x, y) = A\phi_s\phi_r|\nabla\phi_s||\nabla\phi_r|$ is zero outside the interface layer. To match the surface tension of the sharp-interface model, the constant $A = 30/B$ satisfies $\int_{-\infty}^{\infty} W\mathrm{d}y = 1$. The surface tension coefficient $\gamma(x, y)$ decreases linearly with solute concentration $c(x, y)$ under dilute conditions, modelled as $\gamma = 1 - Ca\,c$, where Ca is the capillary number. We choose the viscosity ratio $\zeta_\eta = 1$ and diffusivity ratio $\zeta_D = 1$ to isolate the Marangoni instability that driven by property ratios (Sternling & Scriven 1959), thus the defined coefficients $\eta = \phi_s + (\phi_r/\zeta_\eta) = 1$ and $D = \phi_s + (\phi_r/\zeta_D) = 1$. Gravity is neglected and density ratio is unity.

The dimensionless groups appearing in the equations (2.2a) are Schmidt number $Sc = \eta_s/(\rho_s D_s)$, capillary number $Ca = U\eta_s/\gamma_0$ and Marangoni number $Ma = UL/D_s$, where η_s, ρ_s, and D_s are the viscosity, density, and diffusivity of the phase ϕ_s, respectively. The characteristic velocity is defined as the Marangoni flow $U = \beta|G_c|L/\eta_s$ that prevails in the stationary flow, with $G_c = \Delta c/(4L)$, $\beta = \mathrm{d}\gamma/\mathrm{d}c$. The Péclet number for the phase field is given by $Pe_\phi = UL/M_\phi$, which characterises the competition between advective deformation of the interface and its relaxation toward the equilibrium profile through diffusive processes. The interfacial mobility is set as $M_\phi \propto \delta^\alpha$, with an optimal scaling parameter of $\alpha \approx 1.7$ as recommended in previous studies (Demont *et al.* 2023).

The governing equations ((2.1), (2.2)) are linearised around a base state $\boldsymbol{Q}^b = (\boldsymbol{U}^b, P^b, C^b, \phi_s^b)^T$ with zero velocity $\boldsymbol{U}^b = \boldsymbol{0}$, uniform pressure $P^b = \mathrm{const}$, an equilibrium phase field $\phi_s^b = \phi_{eq}$, and a steady solute gradient $C^b = G_c(H - y)$, where the superscript b denotes the base state of the state vector $\boldsymbol{q} = (\boldsymbol{u}, p, c, \phi_s)^T$. The perturbations $\boldsymbol{q}' = (\boldsymbol{u}', p', c', \phi_s')^T$ are assumed to take the form $\tilde{\boldsymbol{q}}(y)\mathrm{e}^{\mathrm{i}kx - \mathrm{i}\omega t} + \mathrm{c.c.}$, where $\tilde{\boldsymbol{q}} = (\tilde{\boldsymbol{u}}, \tilde{p}, \tilde{c}, \tilde{\phi}_s)^T$ is the state vector of eigenfunctions in a Fourier space, k is the wavenumber, and $\omega = \omega_r + \mathrm{i}\omega_i$ is the complex frequency. A positive growth rate ($\omega_i > 0$) indicates linear instability, while $\omega_i < 0$ implies stability. The real part ω_r represents the oscillation frequency. This leads to a generalised eigenvalue problem of the form, $\omega\widetilde{\boldsymbol{M}}\tilde{\boldsymbol{q}} = \widetilde{\boldsymbol{L}}\tilde{\boldsymbol{q}}$, where $\widetilde{\boldsymbol{M}}$ and $\widetilde{\boldsymbol{L}}$ are linear operators derived from the linearised equations as follows:

$$-\mathrm{i}\omega\tilde{\phi}_s = -\frac{\mathrm{d}\phi_s^b}{\mathrm{d}y}\tilde{v} + \frac{1}{Pe_\phi}\frac{\mathrm{d}^2}{\mathrm{d}y^2}\tilde{\phi}_s - \frac{B}{Pe_\phi}\left[\left(2\phi_s^b - 1\right)\frac{\partial\tilde{\phi}_s}{\partial y} + 2\frac{\mathrm{d}\phi_s^b}{\mathrm{d}y}\tilde{\phi}_s\right], \tag{2.3a}$$

$$-\mathrm{i}\omega\tilde{c} = -\frac{\mathrm{d}C^b}{\mathrm{d}y}\tilde{v} + \frac{1}{Ma}\left(\frac{\mathrm{d}^2}{\mathrm{d}y^2} - k^2\right)\tilde{c}, \tag{2.3b}$$

$$-\mathrm{i}\omega\tilde{u} = \frac{Sc}{Ma}\left[-\mathrm{i}k\tilde{p} + \left(\frac{\mathrm{d}^2}{\mathrm{d}y^2} - k^2\right)\tilde{u} + \frac{W^b}{Ca}\frac{1}{|\nabla\phi_s^b|}\frac{\mathrm{d}\Gamma^b}{\mathrm{d}y}\mathrm{i}k\tilde{\phi}_s - \mathrm{i}k\tilde{c}W^b\right], \tag{2.3c}$$

https://doi.org/10.1017/jfm.2025.10895 Published online by Cambridge University Press

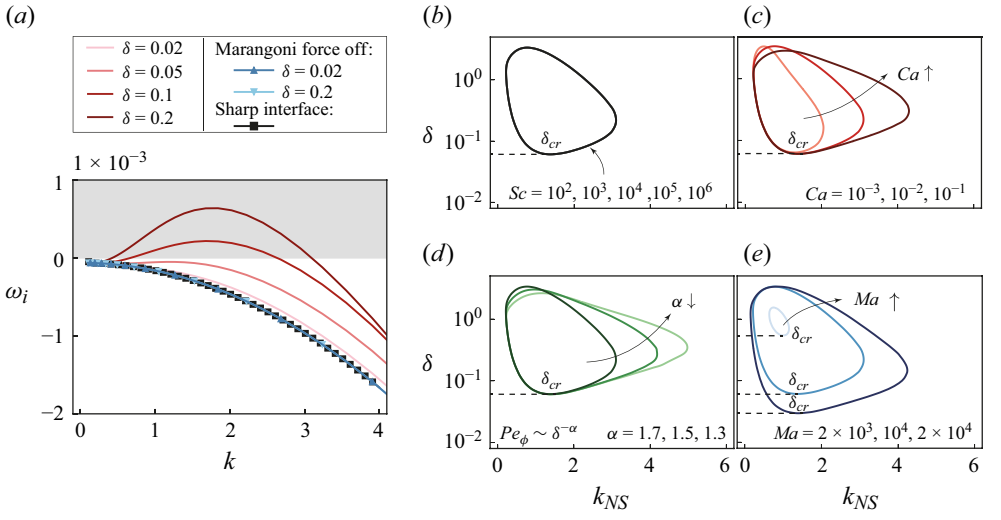


Figure 2. (*a*) Growth rate ω_i versus wavenumber k for different δ. The grey-shaded area indicates $\omega_i > 0$, i.e. instability. Stability is restored when Marangoni force is off. Parameters are $Ma = 10^4$, $Ca = 0.01$, $\alpha = 1.7$. The black solid line with square markers shows the corresponding sharp-interface result. (*b–e*) Instability intervals (enclosed regions) under varying Sc, Ca, Pe_ϕ, and Ma, respectively.

$$-\mathrm{i}\omega\tilde{v} = \frac{Sc}{Ma}\left[-\frac{\partial\tilde{p}}{\partial y} + \left(\frac{\mathrm{d}^2}{\mathrm{d}y^2} - k^2\right)\tilde{v} + \frac{W^b}{Ca}\frac{1}{|\nabla\phi_s^b|}\Gamma^b(-k^2)\tilde{\phi}_s\right], \tag{2.3d}$$

$$0 = \mathrm{i}k\tilde{u} + \frac{\partial\tilde{v}}{\partial y}, \tag{2.3e}$$

where the base state of surface tension $\Gamma^b = 1 - CaC^b$ and weight function $W^b = A\phi_s^b(1-\phi_s^b)|\nabla\phi_s^b|^2$. We refer the reader to Li *et al.* (2025) for the detailed derivation.

3. Results and discussions

3.1. *Unveiling instabilities in diffuse interfaces*

We identify an instability that arises solely in diffuse interfaces and is absent in the sharp-interface limit, driven by Marangoni stresses. We term this the diffuse-interface Marangoni instability.

As shown in figure 2(*a*), short-wavelength instabilities emerge when the interface has finite thickness, even under conditions where sharp-interface theory predicts stability (equal viscosity and diffusivity in both phases) (Sternling & Scriven 1959; Schwarzenberger *et al.* 2014). For $Ma = 10^4$, $Ca = 0.01$, $\alpha = 1.7$ and $Sc = 1000$, an unstable band appears at $\delta = 0.2$ and narrows as δ decreases, disappearing entirely as δ approaches 0.02 – an estimated sharp-interface limit. This limit is calculated by using 'pyoomph' (Diddens & Rocha 2024), following the methodology described in Bauer, Frink & Kreckel (2002), Heil & Hazel (2006). Disabling Marangoni stresses by omitting the $-\mathrm{i}k\tilde{c}W^b$ term in (2.3*c*) suppresses the instability, yielding a single δ-independent growth curve (blue triangles in figure 2*a*), which agrees well with the sharp-interface limit. This confirms that the observed instability stems from solutal Marangoni effects rather than numerical artefacts.

https://doi.org/10.1017/jfm.2025.10895 Published online by Cambridge University Press

To probe the instability mechanism, we vary key parameters individually: Marangoni number $Ma \in [10^3, 10^5]$, capillary number $Ca \in [10^{-3}, 10^{-1}]$, Schmidt number $Sc \in [10^2, 10^6]$ and mobility index $\alpha \in [1.3, 1.7]$. These span $Re \in [10^{-2}, 10^2]$ and $Pe_\phi \in [0.3, 1.6 \times 10^5]$, with $Re = Ma/Sc$ and $Pe_\phi = UL/\delta^\alpha$. Default parameters are $Ma = 10^4$, $Ca = 0.01$, $\alpha = 1.5$ and $Sc = 1000$, chosen based on typical physical values to ensure realistic, weakly deformed interfaces, with α set according to established recommendations (Jacqmin 1999; Magaletti *et al.* 2013).

Figure 2(*b–e*) shows the neutral stability curves k_{NS} versus interfacial thickness δ. Here, Sc has little influence, consistent with prior studies (Reichenbach & Linde 1981; Li *et al.* 2025). Accordingly, inertia is negligible for the instability threshold within the Re studied range ($Re = 0.01$–100). In contrast, Ma, Ca and $Pe_\phi \sim \delta^{-\alpha}$ significantly alter the instability. Lower Ca or higher α suppresses short-wavelength modes but leaves the critical thickness δ_{cr} unchanged. In contrast, reducing Ma narrows the unstable wavenumber band and increases δ_{cr}, shrinking the unstable regime. These results indicate that while δ, Ma, Ca and Pe_ϕ govern instability onset, δ_{cr} is uniquely determined by Ma.

3.2. *Scaling laws for critical diffuse-interface thickness*

In the laminar regime, the critical thickness δ_{cr} depends uniquely on Ma, not Ca or Pe_ϕ, indicating that δ_{cr} is governed primarily by solutal Marangoni advection–diffusion dynamics near the interface ((2.2*b*) and (2.3*b*)). The circulation (figure 1*b*) transports solute toward the interface, steepening concentration gradients, while diffusion tends to smooth them. This competition features the Marangoni interfacial flows (Manikantan & Squires 2020). Since advection in the normal direction transports fluids of different concentrations across the layers, δL is taken as the characteristic length scale. Balancing diffusion (time scale $t_D \sim (\delta L)^2/D$) and advection ($t_A \sim \delta L/U$) yields the scaling

$$\delta_{cr} \sim Ma^{-1}. \tag{3.1}$$

As Ma increases, stronger advection requires a thinner interface to maintain stability. This Ma–δ_{cr} scaling is confirmed as $\delta_{cr} \to 0$ in figure 3(*a*), and remains robust under changes in Ca or Pe_ϕ, as shown in figures 2(*c*) and 2(*d*). This relation provides a physical criterion for selecting δ in diffuse-interface simulations with Marangoni effects, ensuring convergence to the sharp-interface limit (Jacqmin 1999). While thin-interface limit criteria exist for passive two-phase flows (Magaletti *et al.* 2013; Demont *et al.* 2023), the present finding extends them to Marangoni-driven instabilities, consistent with thermocapillary flow observations by Verschueren *et al.* (2001).

To explain the deviation from the scaling law (3.1) at larger interfacial thickness (i.e. for $Ma \lesssim 4000$), we perform an energy-based analysis to quantify the competing mechanisms. Multiplying the linearised perturbation equations ((2.3*c*) and (2.3*d*)) by the velocity perturbations yields an energy budget:

$$\begin{aligned}\frac{\partial E_{kin}}{\partial t} = &\underbrace{\frac{1}{Re}\left[-\left(\nabla u'\right)^2 - \left(\nabla v'\right)^2\right]}_{\mathcal{E}_\eta:\ \text{Viscous dissipation}} + \underbrace{\frac{1}{Re}\frac{1}{Ca}\left[\frac{\Gamma^b}{\left|\nabla \phi_s^b\right|}\frac{\partial^2 \phi_s'}{\partial x^2}v'\right]W^b}_{\mathcal{E}_\gamma^{cap}:\ \text{Capillary effect}} \\ &+ \underbrace{\frac{1}{Re}\frac{1}{Ca}\left[\frac{1}{\left|\nabla \phi_s^b\right|}\frac{\partial \phi_s'}{\partial x}\frac{\mathrm{d}\Gamma^b}{\mathrm{d}y}u'\right]W^b}_{\mathcal{E}_\gamma^{tilt}:\ \text{Tilt-induced Marangoni}} + \underbrace{\frac{1}{Re}\left[-\frac{\partial c'}{\partial x}u'\right]W^b}_{\mathcal{E}_\gamma^{mag}:\ \text{Solutal Marangoni effect}}.\end{aligned} \tag{3.2}$$

https://doi.org/10.1017/jfm.2025.10895 Published online by Cambridge University Press

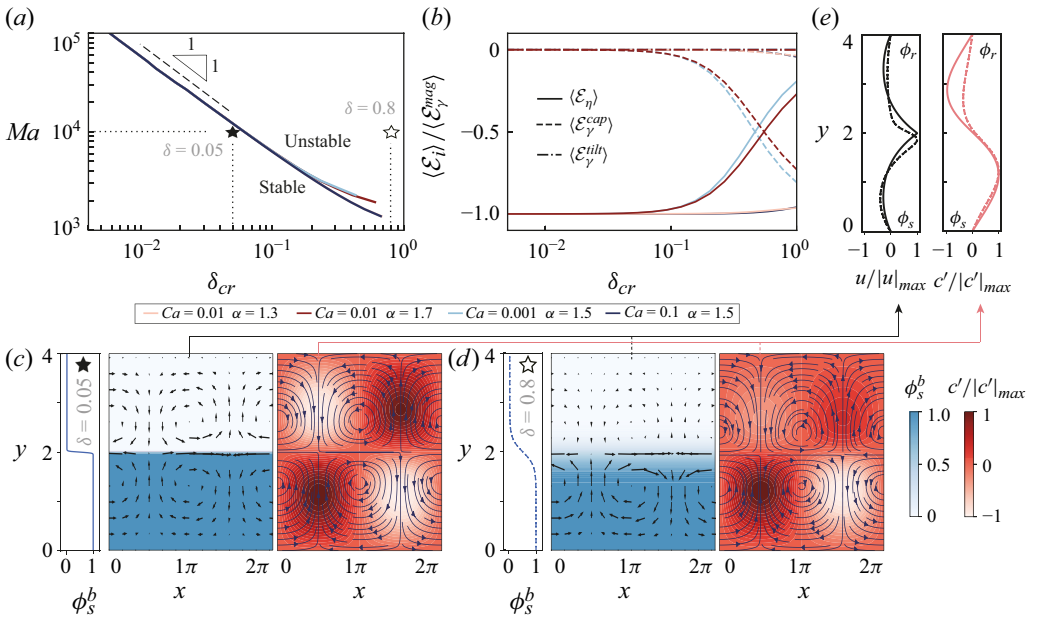


Figure 3. (*a*) Scaling of the critical interface thickness δ_{cr} with Ma, showing $\delta_{cr} = 590/Ma$ for $Ma \gtrsim 4000$, independent of Ca and α. Deviations from the scaling emerge with increasing α or decreasing Ca. (*b*) Energy budget showing the relative contributions of $\langle \mathcal{E}_i \rangle = \langle \mathcal{E}_\eta \rangle$ (viscous dissipation), $\langle \mathcal{E}_\gamma^{cap} \rangle$ (capillary forces), $\langle \mathcal{E}_\gamma^{tilt} \rangle$ (interfacial tilt), compared to the solutal Marangoni effect $\langle \mathcal{E}_\gamma^{mag} \rangle$, as δ_{cr} increases. (*c*,*d*) Base-state phase field ϕ_s^b and solute perturbation c' for the stable case ($\delta = 0.05$) and unstable case ($\delta = 0.8$). Velocity vectors are overlaid on ϕ_s^b; streamlines are shown in c'. The temporal evolutions from DNS are given in supplementary movies S1 and S2, respectively, available at https://doi.org/10.1017/jfm.2025.10895. (*e*) Cross-sectional profiles of u (at $x = \pi$) and c' (at $x = \pi/2$) along the y-direction for the stable (solid lines) and unstable (dashed lines) cases.

Here, the kinetic energy density is defined as $E_{kin} = (u'^2 + v'^2)/2$, since the base flow $\boldsymbol{U}^b$ is zero and total velocity reduces to the perturbation field ($\boldsymbol{u} = \boldsymbol{u}'$). The prefactor Ma/Sc is replaced by $Re \lesssim 4$.

The viscous dissipation $\mathcal{E}_\eta$ reflects energy loss due to shear. The solutal Marangoni term $\mathcal{E}_\gamma^{mag}$ originates from tangential solute gradients $-\partial c'/\partial x$. The capillary term $\mathcal{E}_\gamma^{cap}$ arises from interface curvature and base-state tension Γ^b. The tilt-induced Marangoni term $\mathcal{E}_\gamma^{tilt}$ stems from interfacial tilt $\partial \phi_s'/\partial x$, which projects normal interfacial tension gradients $\mathrm{d}\Gamma^b/\mathrm{d}y$ across the diffuse layer (Berry 1971; Marchand *et al.* 2011) onto the tangential direction – an effect inherently tied to the finite thickness of diffuse interfaces and absent in sharp-interface models.

Along the Ma–δ_{cr} paths (figure 3*a*), integrating over the domain $[2\pi/k \times 4L]$ gives the power balance $\langle \mathcal{E}_\eta \rangle + \langle \mathcal{E}_\gamma^{cap} \rangle + \langle \mathcal{E}_\gamma^{tilt} \rangle + \langle \mathcal{E}_\gamma^{mag} \rangle = 0$ ($\omega_i = 0$), where the angled brackets $\langle \cdot \rangle$ denote a spatial average over the entire computational domain. Divergence terms vanish under periodic, homogeneous boundary conditions (Zhang *et al.* 2013). Figure 3(*b*) shows the normalised contributions of each term by $\langle \mathcal{E}_\gamma^{mag} \rangle$ as δ_{cr} increases. For small δ_{cr} ($\lesssim 0.1$), the balance is primarily between viscous dissipation $\mathcal{E}_\eta$ and solutal Marangoni forcing $\mathcal{E}_\gamma^{mag}$, consistent with the scaling law. As δ_{cr} increases, the influence of capillary $\mathcal{E}_\gamma^{cap}$ starts at a certain δ_{cr}, beyond which deviations from the ideal $\delta_{cr} \sim Ma^{-1}$ scaling become significant. Thus, interface deformation affects the limits of the scaling law's validity.

https://doi.org/10.1017/jfm.2025.10895 Published online by Cambridge University Press

Figures 3(*c*) and 3(*d*) show the base-state phase field ϕ_s^b (blue), velocity field $\boldsymbol{u} = \boldsymbol{u}'$ (arrows) normalised by its global maximum absolute value $|u|_{max}$, and perturbation concentration field c' (red) normalised by its global maximum absolute value $|c'|_{max}$ for two representative cases: a stable system ($\delta = 0.05$) and an unstable one ($\delta = 0.8$), corresponding to the solid and open star symbols in figure 3(*a*), respectively. In the stable case (figure 3*c*), vortices are symmetrically distributed about the interface, as evidenced by the velocity component u profiles at $x = \pi$ (figure 3*e*, black solid line). This balanced Marangoni recirculation gives rise to an anti-symmetric c' field, confirmed by the profile at $x = \pi/2$ (figure 3*e*, red solid line). In contrast, the unstable case (figure 3*d*) exhibits anti-symmetry breaking, with flow field shifting downward into source phase (figure 3*e*, black dashed line). The zero-crossing point of c' shifts upward from the interface centreline ($y = 2$), indicating solute enrichment in the receiver phase and depletion in the source phase (figure 3*e*, red dashed line). We further performed DNS (Li *et al.* 2025) for both cases to reveal the evolution of the different fields, with the results provided in the supplementary movies. These symmetry-breaking shifts in both velocity and concentration profiles motivate the next section, in which we investigate their physical origin and impact on the instability.

3.3. *Mechanism of instability in diffuse interfaces: anti-flux versus pro-flux shifts*

In classical sharp-interface systems with equal viscosity and diffusivity between two fluids, interfacial Marangoni instability is absent (Sternling & Scriven 1959). As illustrated in figure 4(*a*), symmetric convection brings high (C^H) and low (C^L) concentrations toward the interfacial stagnation point. Equal diffusivity and viscosity ensure that net interfacial concentration remains unchanged, yielding no amplification of the Marangoni flow u_m. In contrast, a diffuse interface introduces local asymmetry. Figure 4(*b*) shows that inflow of low-concentration fluid reduces interfacial concentration C^- on the receiver phase ϕ_r side, while inflow of high-concentration fluid increases C^+ on the source ϕ_s side. Within the interfacial layer of thickness δ, the resulting imbalance cannot be instantly homogenised, leading to a tangential concentration gradient $\nabla_s C(y)$ and an associated velocity profile $u(y)$.

As shown in figure 4(*c*), the local concentration decrease on the receiver side (ϕ_r) reduces the interfacial tension gradient $(\nabla_s \gamma)^-$, thereby weakening the Marangoni flow (Anderson *et al.* 1998). Conversely, the increased concentration on the source side (ϕ_s) enhances $(\nabla_s \gamma)^+$, strengthening the flow. This asymmetry in surface tension gradients induces a shear layer within the interface, with suppressed velocity near ϕ_r and enhanced velocity near ϕ_s. The resulting shear promotes an interfacial instability reminiscent of, yet physically distinct from, the classical Kelvin–Helmholtz instability (Chandrasekhar 2013), since the present mechanism arises from Marangoni-driven shear within a diffuse interface rather than inertia-dominated interfacial waves. This asymmetry in surface tension gradients induces a shear layer within the interface, with suppressed velocity near ϕ_r and enhanced velocity near ϕ_s. We quantify the shift of the peak velocity (u_m) position y_{u_m} away from the interface centreline ($y = 2L$) by the anti-flux offset, $\ell_\delta^u = 2L - y_{u_m}$, which characterises the destabilising effect of advection-driven shear. Diffusion counters this destabilisation by smoothing concentration gradients ($C^- \uparrow$ and $C^+ \downarrow$), as depicted in figure 4(*d*). The position y_{C^0} where the net concentration change vanishes (C^0) shifts along the solute flux into the receiver side. This stabilising effect is captured by the pro-flux offset $\ell_\delta^{c'} = y_{C^0} - 2L$. Figures 4(*e*) and 4(*f*) illustrate the evolution of the velocity and concentration profiles within the diffuse interface at three representative instants, as obtained from DNS of the unstable case ($\delta = 0.8$), thereby confirming the mechanisms discussed.

https://doi.org/10.1017/jfm.2025.10895 Published online by Cambridge University Press

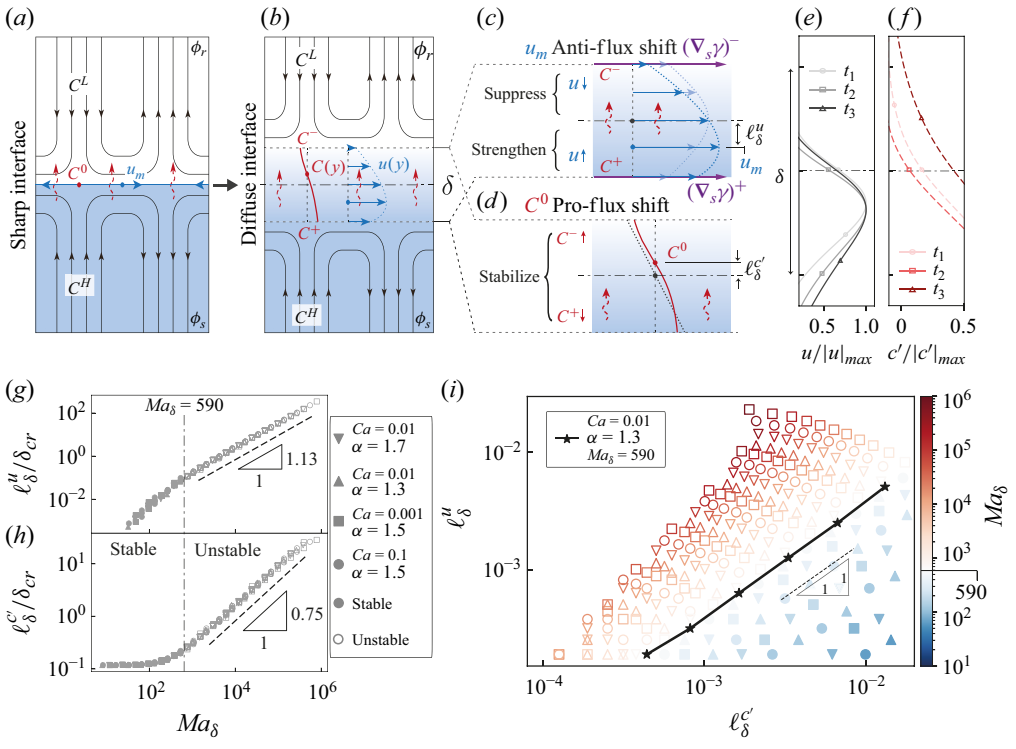


Figure 4. (*a*) Schematic of interfacial solute and velocity fields in the sharp-interface limit, where symmetric advection yields no net concentration change. (*b*) Profiles of solute concentration $C(y)$ and tangential velocity $u(y)$ across the diffuse interface. (*c*) Mechanism of velocity offset ℓ_δ^u: asymmetric solute advection enhances Marangoni flow on the source side, displacing the velocity peak away from the centreline. (*d*) Mechanism of solute offset $\ell_\delta^{c'}$: coupled vertical flow and interfacial diffusion shift the position of zero net solute change. (*e*,*f*) Cross-sectional profiles of u and c' for the unstable case ($\delta = 0.8$) at three representative times ($t_1 = 10^4$, $t_2 = 5 \times 10^4$ and $t_3 = 16 \times 10^4$) from DNS, showing the offsets ℓ_δ^u and $\ell_\delta^{c'}$. Here, u and c' are normalised by their global maximum absolute values $|u|_{max}$ and $|c'|_{max}$, respectively. (*g*,*h*) Normalised offsets $\ell_\delta^u/\delta_{cr}$ and $\ell_\delta^{c'}/\delta_{cr}$ versus the modified Marangoni number $Ma_\delta = Ma\,\delta$, showing collapse across varying Ca and α. Instability sets in at $Ma_{cr}^\delta \approx 590$. (*i*) Phase diagram in the ℓ_δ^u–$\ell_\delta^{c'}$ plane. Stable (solid) and unstable (open) regimes are separated by the scaling $\ell_\delta^u \sim (\ell_\delta^{c'})$.

To quantify the competition between advection and diffusion across the interface, we introduce a modified Marangoni number $Ma_\delta = Ma\,\delta$, using the interfacial thickness $\hat{\delta}$ as the characteristic length scale. As shown in figures 4(*g*) and 4(*h*), both the velocity offsets ℓ_δ^u and the concentration offset $\ell_\delta^{c'}$ increase monotonically with Ma_δ, following distinct power-law trends that collapse across different $Ca \in [10^{-3}, 10^{-1}]$ and $\alpha \in [1.3, 1.7]$, confirming their universality. A critical transition emerges at $Ma_\delta \approx 590$: below this threshold, the system remain stable, with ℓ_δ^u growing sublinearly and $\ell_\delta^{c'}$ superlinearly; beyond it, the system becomes unstable, and both offsets grow with fixed exponents, approximately 1.13 for ℓ_δ^u and 0.75 for $\ell_\delta^{c'}$.

To further capture this interplay, figure 4(*i*) plots ℓ_δ^u against $\ell_\delta^{c'}$, revealing a clear separation between stable (bluish solid) and unstable (reddish open) regimes by the power-law relation $\ell_\delta^u \sim (\ell_\delta^{c'})^m$. The critical exponent $m = 1$ at $Ma_\delta = 590$ (black solid line with star symbols) marks a crossover from diffusion-dominated stabilisation ($m < 1$)

https://doi.org/10.1017/jfm.2025.10895 Published online by Cambridge University Press

to advective-driven destabilisation ($m > 1$), highlighting the offset competition as the underlying mechanism governing interfacial instability.

4. Conclusion

We have uncovered a Marangoni-induced diffuse-interface instability that is absent in the sharp-interface limit. Through linearised analysis of a validated phase-field NSAC model, we show that finite interfacial thickness introduces asymmetric solute distributions and tangential velocity shifts that destabilise the interface, even in fluids with matched viscosity and diffusivity. A critical interfacial thickness $\delta_{cr} \sim Ma^{-1}$ emerges from the competition between diffusive and advective time scales. Energy analysis reveals that deviations at large δ_{cr} arise from interface deformation and asymmetric tension projection. By introducing a modified Marangoni number $Ma_\delta = Ma\delta$, we reveal universal power-law behaviour in velocity and concentration offsets, independent of Ca and α (Pe_ϕ). The crossover at $Ma_\delta \approx 590$, where the exponent $\ell_\delta^u \sim (\ell_\delta^{c'})^m$ with $m = 1$, marks the transition from diffusive stabilisation to advective destabilisation.

These findings not only clarify the physical origin of instability in diffuse interfaces but also provide a predictive framework for multicomponent multiphase systems where sharp-interface assumptions fail. Potential experimental systems include miscible liquid–liquid interfaces, where relaxing interfaces exhibit a measurable effective interfacial tension across a wide range of fluids (Truzzolillo & Cipelletti 2017). This work opens new directions for studying interfacial transport in miscible fluids, soft materials and microfluidic systems (Shim 2022; Michelin 2023; Ault & Shin 2025), where interfacial thickness and multi-physics coupling critically influence dynamics

Supplementary movies. Supplementary movies are available at https://doi.org/10.1017/jfm.2025.10895.

Funding. H.T. acknowledges support from the National Natural Science Foundation of China (grant nos 12472271, 12102171) and the Guangdong Basic and Applied Basic Research Foundation (grant no. 2024A1515010614). M.Z. acknowledges support from the Ministry of Education, Singapore (WBS no. A-8001172-00-00).

Declaration of interests. The authors report no conflict of interest.

References

Anderson, D.M., McFadden, G.B. & Wheeler, A.A. 1998 Diffuse-interface methods in fluid mechanics. *Annu. Rev. Fluid Mech.* **30** (1), 139–165.

Ault, J.T. & Shin, S. 2025 Physicochemical hydrodynamics of particle diffusiophoresis driven by chemical gradients. *Annu. Rev. Fluid Mech.* **57**, 227255.

Bauer, C., Frink, A. & Kreckel, R. 2002 Introduction to the ginac framework for symbolic computation within the c++ programming language. *J. Symb. Comput.* **33** (1), 1–12.

Bergfreund, J., Diener, M., Geue, T., Nussbaum, N., Kummer, N., Bertsch, P., Nyström, G. & Fischer, P. 2021 Globular protein assembly and network formation at fluid interfaces: effect of oil. *Soft Matter* **17** (6), 1692–1700.

Berry, M.V. 1971 The molecular mechanism of surface tension. *Phys. Educ.* **6** (2), 79.

Cahn, J.W. & Hilliard, J.E. 1958 Free energy of a nonuniform system. i. interfacial free energy. *J. Chem. Phys.* **28** (2), 258–267.

Chandrasekhar, S. 2013 *Hydrodynamic and Hydromagnetic Stability*. Courier Corporation.

Darhuber, A.A. & Troian, S.M. 2003 Marangoni driven structures in thin film flows. In *Gallery of Fluid Motion*, p. S9.

Demont, T. H. B., Stoter, S. K. F. & Van Brummelen, E. H. 2023 Numerical investigation of the sharp-interface limit of the Navier–Stokes–Cahn–Hilliard equations. *J. Fluid Mech.* **970**, A24.

Diddens, C., Dekker, P.J. & Lohse, D. 2024 Non-monotonic surface tension leads to spontaneous symmetry breaking in a binary evaporating drop, arXiv preprint arXiv:2402.17452.

https://doi.org/10.1017/jfm.2025.10895 Published online by Cambridge University Press

DIDDENS, C. & ROCHA, D. 2024 Bifurcation tracking on moving meshes and with consideration of azimuthal symmetry breaking instabilities. *J. Comput. Phys.* **518**, 113306.
ECKERT, K., ACKER, M., TADMOURI, R. & PIMIENTA, V. 2012 Chemo-Marangoni convection driven by an interfacial reaction: pattern formation and kinetics. *Chaos: Interdiscipl. J. Nonlinear Sci.* **22** (3), 037112.
HAO, H., LI, X., LIU, T. & TAN, H. 2025 Enhanced profile-preserving phase-field model of two-phase flow with surfactant interfacial transport and marangoni effects. *J. Comput. Phys.* 114058.
HAO, H., LI, X., XU, L., LIU, T. & TAN, H. 2026 Profile-preserving phase-field model for surfactant transport and adsorption–desorption in two-phase flow systems. *J. Comput. Phys.* **546**, 114510.
HEIL, M. & HAZEL, A.L. 2006 Oomph-lib – an object-oriented multi-physics finite-element library. In *Fluid-Structure Interaction* (ed. H.-J. Bungartz & M. Schäfer), pp. 19–49. Springer.
JACQMIN, D. 1999 Calculation of two-phase navier stokes flows using phase-field modeling. *J. Comput. Phys.* **155** (1), 96–127.
JOSEPH, D.D., RENARDY, Y.Y., JOSEPH, D.D. & RENARDY, Y.Y. 1993 Fluid dynamics of two miscible liquids with diffusion and gradient stresses. In *Fundamentals of Two-Fluid Dynamics: Part II: Lubricated Transport, Drops and Miscible Liquids*, pp. 324–395.
KOVALCHUK, N. & VOLLHARDT, D. 2006 Marangoni instability and spontaneous non-linear oscillations produced at liquid interfaces by surfactant transfer. In *Advances in Colloid and Interface Science*.
LEVICH, V. G. & KRYLOV, V. S. 1969 Surface-tension-driven phenomena. *Annu. Rev. Fluid Mech.* **1** (1), 293–316.
LI, X., WAN, D., ZHANG, M. & TAN, H. 2025 Marangoni interfacial instability induced by solute transfer across liquid–liquid interfaces. *Int. J. Multiphas. Flow* **184**, 105073.
LIU, C., YANG, J., GUO, B.-B., AGARWAL, S., GREINER, A. & Z.-K., XU 2021 Interfacial polymerization at the alkane/ionic liquid interface. *Angew. Chem-GER. Edit.* **133** (26), 14757–14764.
LOHSE, D. & ZHANG, X. 2020 Physicochemical hydrodynamics of droplets out of equilibrium. *Nat. Rev. Phys.* **2** (8), 426–443.
MAGALETTI, F., PICANO, F., CHINAPPI, M., MARINO, L. & CASCIOLA, C. M. 2013 The sharp-interface limit of the Cahn–Hilliard/Navier–Stokes model for binary fluids. *J. Fluid Mech.* **714**, 95–126.
MANIKANTAN, H. & SQUIRES, T.M. 2020 Surfactant dynamics: hidden variables controlling fluid flows. *J. Fluid Mech.* **892**, P1.
MARCHAND, A., WEIJS, J.H., SNOEIJER, J.H. & ANDREOTTI, B. 2011 Why is surface tension a force parallel to the interface? *Am. J. Phys.* **79** (10), 999–1008.
MICHELIN, S. 2023 Self-propulsion of chemically active droplets. *Annu. Rev. Fluid Mech.* **55** (1), 77–101.
MITRA, S., SINGH, S.K., SHEVCHENKO, E., SACHAN, M., GHOSH, A., BASAK, M., PATTADER, G. & SARATHI, P. 2020 Efficient microextraction process exploiting spontaneous interfacial convection driven by marangoni and electric field induced instability: a computational fluid dynamics study. *Phys. Fluids* **32** (1), 014102.
MITRINOVIĆ, D.M., TIKHONOV, A.M., LI, M., HUANG, Z. & SCHLOSSMAN, M.L. 2000 Noncapillary-wave structure at the water-alkane interface. *Phys. Rev. Lett.* **85** (3), 582.
RAYLEIGH, L. 1892 Xx. On the theory of surface forces—ii. Compressible fluids. *Lond., Edinb., Dublin Philos. Mag. J. Sci.* **33** (201), 209–220.
REDER, M., PRAHS, A., SCHNEIDER, D. & NESTLER, B. 2024 Viscous stress approximations in diffuse interface methods for two-phase flow based on mechanical jump conditions. *Comput. Methods Appl. Mech.* **432**, 117341.
REICHENBACH, J. & LINDE, H. 1981 Linear perturbation analysis of surface-tension-driven convection at a plane interface (marangoni instability). *J. Colloid Interf. Sci.* **84** (2), 433–443.
RUCKENSTEIN, E. & BERBENTE, C. 1964 The occurrence of interfacial turbulence in the case of diffusion accompanied by chemical reaction. *Chem. Eng. Sci.* **19** (5), 329–347.
SCARDOVELLI, R. & ZALESKI, S. 1999 Direct numerical simulation of free-surface and interfacial flow. *Annu. Rev. Fluid Mech.* **31** (1), 567–603.
SCHWARZENBERGER, K., KÖLLNER, T., LINDE, H., BOECK, T., ODENBACH, S. & ECKERT, K. 2014 Pattern formation and mass transfer under stationary solutal Marangoni instability. *Adv. Colloid Interfac.* **206**, 344–371.
SCRIVEN, L. E. 1960 Dynamics of a fluid interface equation of motion for Newtonian surface fluids. *Chem. Eng. Sci.* **12** (2), 98–108.
SENAPATI, S. & BERKOWITZ, M.L. 2001 Computer simulation study of the interface width of the liquid/liquid interface. *Phys. Rev. Lett.* **87** (17), 176101.
SHIM, S. 2022 Diffusiophoresis, diffusioosmosis, and microfluidics: surface-flow-driven phenomena in the presence of flow. *Chem. Rev.* **122** (7), 6986–7009.
STANLEY, H.E. 1971 *Introduction to Phase Transitions and Critical Phenomena*. Oxford University Press.

https://doi.org/10.1017/jfm.2025.10895 Published online by Cambridge University Press

STERNLING, C. V. & SCRIVEN, L. E. 1959 Interfacial turbulence: hydrodynamic instability and the marangoni effect. *Aiche J.* **5** (4), 514–523.

SULTAN, E., BOUDAOUD, A. & AMAR, M.B. 2005 Evaporation of a thin film: diffusion of the vapour and marangoni instabilities. *J. Fluid Mech.* **543**, 183–202.

TAN, H., DIDDENS, C., LV, P., KUERTEN, J.G.M., ZHANG, X. & LOHSE, D. 2016 Evaporation-triggered microdroplet nucleation and the four life phases of an evaporating ouzo drop. *Proc. Natl. Acad. Sci.* **113** (31), 8642–8647.

TRUZZOLILLO, D. & CIPELLETTI, L. 2017 Off-equilibrium surface tension in miscible fluids. *Soft Matter* **13**(1), 13–21.

VERSCHUEREN, M., VAN DE VOSSE, F. N. & MEIJER, H. E. H. 2001 Diffuse-interface modelling of thermocapillary flow instabilities in a Hele–Shaw cell. *J. Fluid Mech.* **434**, 153–166.

VAN DER WAALS, J. 1893 Verhandel. konink. akad. weten. amsterdam (sect1). *Philos. Mag.* **1**, 56.

ZHANG, M., LASHGARI, I., ZAKI, T.A. & BRANDT, L. 2013 Linear stability analysis of channel flow of viscoelastic Oldroyd-B and FENE-P fluids. *J. Fluid Mech.* **737**, 249–279.

https://doi.org/10.1017/jfm.2025.10895 Published online by Cambridge University Press